Influence of an Electric-field on the Topological Stability of the Neutral Lithium Dimer

Xinxin Feng[1], Alireza Azizi[2], Tianlv Xu[1], Wenjing Yu[1], Xiaopeng Mi[1], Hui Lu[1], Herbert Früchtl[3], Tanja van Mourik[3], Steven R. Kirk[*1] and Samantha Jenkins[*1]

[1]Key Laboratory of Chemical Biology and Traditional Chinese Medicine Research and Key Laboratory of Resource National and Local Joint Engineering Laboratory for New Petro-chemical Materials and Fine Utilization of Resources, College of Chemistry and Chemical Engineering, Hunan Normal University, Changsha, Hunan 410081, China

[2]State Key Laboratory of Powder Metallurgy, School of Materials Science & Engineering, Central South University, Changsha, Hunan 410083, China

[3]EaStCHEM School of Chemistry, University of Saint Andrews, North Haugh, St Andrews, Fife KY16 9ST, Scotland, United Kingdom.

Email : steven.kirk@cantab.net
Email : samanthajsuman@gmail.com

In this investigation we seek to understand the role of non-nuclear attractors (*NNA*s) of the neutral Li_2 dimer subjected to an electric ($\pm\mathbf{E}$) field that is directed parallel ($\pm\mathbf{E}_x$) and perpendicular ($\pm\mathbf{E}_y$) to the bond-path. The $\pm\mathbf{E}_x$-fields and $\pm\mathbf{E}_y$-fields are separately applied to the Li_2 molecular graph until the bond ruptures. The next generation quantum theory of atoms in molecules (NG-QTAIM) interpretation of bonding was constructed with the stress tensor $\boldsymbol{\sigma}(\mathbf{r})$ eigenvectors on the Hessian of $\rho(\mathbf{r})$ molecular graph. The asymmetry induced by both the $\pm\mathbf{E}_y$-field and $\pm\mathbf{E}_x$-field was detected in terms of the rotation of the orthogonal triad of stress tensor $\boldsymbol{\sigma}(\mathbf{r})$ eigenvectors $\{\underline{\mathbf{e}}_{1\sigma}, \underline{\mathbf{e}}_{2\sigma}, \underline{\mathbf{e}}_{3\sigma}\}$ relative to the Cartesian coordinate frame. The orthogonal triad of Hessian of $\rho(\mathbf{r})$ eigenvectors $\{\underline{\mathbf{e}}_1, \underline{\mathbf{e}}_2, \underline{\mathbf{e}}_3\}$ however, were only able to detect rotation induced by the high degree of asymmetry present for bent bond-paths induced by the $\pm\mathbf{E}_y$-fields. Larger movement of the *NNA*s along the bond-path correlated with greater bond critical point (*BCP*) bond metallicity $\xi(\mathbf{r}_b)$. The effect of applying the $\pm\mathbf{E}_x$-field was compared with unpublished results on neutral Li_2 subject to a stretching distortion. The lack of *NNA* motion along the bond-path for the stretching distortion correlated with a lower degree of bond metallicity $\xi(\mathbf{r}_b)$. The stress tensor $\boldsymbol{\sigma}(\mathbf{r})$ eigenvectors have a unique ability to detect rotation relative to the Cartesian coordinate frame for high bond-path symmetry occurring for the bond-stretching distortion and application of the $\pm\mathbf{E}_x$-field. Suggestions for future work are provided.

1. Introduction

Previously we investigated the presence of non-nuclear attractors (*NNA*s) in small neutral lithium clusters Li_m (m = 2-5) [1]. *NNA*s were found to be present for all relaxed geometries corresponding to the Hessian of the molecular electron density $\rho(\mathbf{r})$, commonly referred to as QTAIM (Quantum Theory of Atoms in Molecules) molecular graphs. None of the corresponding molecular graphs for the Ehrenfest Force $\mathbf{F}(\mathbf{r})$ partitioning contained *NNA*s. This finding is in agreement with a recent thorough investigation by Terrabuio and Teodoro *et al*. where *NNA*s were discovered in all cases for the Hessian of $\rho(\mathbf{r})$ molecular graphs and none were found on any of the Ehrenfest Force $\mathbf{F}(\mathbf{r})$ molecular graphs [2]. This work of Terrabuio and Teodoro *et al*. also provided evidence that a small difference in the polarizability between the Li atoms in the Li_2 cluster is an important feature that favors the occurrence of *NNA*s. The quantum stress tensor $\boldsymbol{\sigma}(\mathbf{r})$, using Bader's definition, was used in our earlier investigation [3], obtained within the QTAIM Hessian of $\rho(\mathbf{r})$ [4] partitioning. The quantum stress tensor $\boldsymbol{\sigma}(\mathbf{r})$ directly relates to the Ehrenfest force $\mathbf{F}(\mathbf{r})$ by the virial theorem and so provides a useful physical explanation into the molecular structural rearrangements that occur during chemical reactions and low frequency normal vibrational modes [5]–[13]. The Ehrenfest Force $\mathbf{F}(\mathbf{r})$ partitioning scheme relates the net force exerted on $\rho(\mathbf{r})$ at a given point $\mathbf{r}$, by summing the forces of attraction by all the nuclei and forces of repulsion by the average electron density [5], [14], thereby providing a physical basis of understanding. As a consequence of the Ehrenfest $\mathbf{F}(\mathbf{r}) = -\nabla\cdot\boldsymbol{\sigma}(\mathbf{r}) = 0$, formed from the dot product ($\cdot$) of the gradient (∇) operator and the stress tensor ($\boldsymbol{\sigma}(\mathbf{r})$) where the position of the stress tensor $\boldsymbol{\sigma}(\mathbf{r})$ bond critical point (*BCP*) will coincide with the Ehrenfest Force $\mathbf{F}(\mathbf{r})$ *BCP*s.

In this investigation we will use next generation QTAIM (NG-QTAIM) [15]. The origins of NG-QTAIM arose from discovering that the $\underline{\mathbf{e}}_2$ and $\underline{\mathbf{e}}_1$ eigenvectors indicate the most and least preferred directions of $\rho(\mathbf{r_b})$ motion, accumulation and subsequent direction of the *BCP* bond displacement[16] when a molecular structure is subjected to an external force or field. In this previous investigation of neutral lithium, the three-stranded interpretation of the bond by NG-QTAIM was used, where the stress tensor $\boldsymbol{\sigma}(\mathbf{r})$ version $\mathbb{B}_{\boldsymbol{\sigma}}$ is constructed using the least preferred ($\underline{\mathbf{e}}_{2\boldsymbol{\sigma}}$) and most preferred ($\underline{\mathbf{e}}_{1\boldsymbol{\sigma}}$) directions of charge density $\rho(\mathbf{r})$ accumulation, along with the bond-path ($\boldsymbol{r}$), obtained from the stress tensor eigenvectors. The $\mathbb{B}_{\boldsymbol{\sigma}}$ was then transplanted on both the Hessian of $\rho(\mathbf{r})$ and Ehrenfest Force $\mathbf{F}(\mathbf{r})$ molecular graphs and compared. We found that the $\mathbb{B}_{\boldsymbol{\sigma}}$ using the stress tensor $\boldsymbol{\sigma}(\mathbf{r})$ eigenvectors on the Hessian of $\rho(\mathbf{r})$ molecular graph was comparable to the $\mathbb{B}_{\boldsymbol{\sigma F}}$ that used the stress tensor $\boldsymbol{\sigma}(\mathbf{r})$ eigenvectors on the Ehrenfest Force $\mathbf{F}(\mathbf{r})$ molecular graph.

We therefore provide a method to examine *NNA*s whilst providing insight from the Ehrenfest Force $\mathbf{F}(\mathbf{r})$ without the difficulty of calculating the Ehrenfest Force $\mathbf{F}(\mathbf{r})$, which requires very large basis sets.

Simple insight into the effect of the *NNA* on the topological stability of the neutral Li_2 dimer was gained by performing a stretching distortion that led to a large increase in the degree of asymmetry of the $\mathbb{B}_{\boldsymbol{\sigma}}$ and $\mathbb{B}_{\boldsymbol{\sigma F}}$, which was apparent as persistent bond-path torsions. Sufficient stretching of the Li_2 bond-path annihilated the

NNA and appeared to increase the degree of bond-path twisting, which led us to hypothesize that prior to rupture the *NNA* provided a topologically stabilizing effect by inhibiting the bond-path twisting.

In the current investigation on neutral Li_2 we will use the stress tensor $\boldsymbol{\sigma}(\mathbf{r})$, which is sensitive to changes in topology, and will use NG-QTAIM to determine the effects of an applied electric ($\pm\mathbf{E}$) field, see **Scheme 1**.

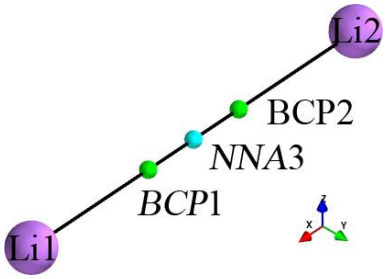

Scheme 1. The numbering scheme of the relaxed structure of the neutral lithium (Li_2) molecular graph is shown, where the purple spheres (Li1 and Li2) represent the lithium nuclear critical points (*NCP*s), the pale-blue sphere (*NNA*3) and green spheres (*BCP*1 and *BCP*2), non–nuclear attractor (*NNA*) and the bond critical points (*BCP*s), respectively. The Cartesian axes correspond to the electric ($\pm\mathbf{E}_x$, $\pm\mathbf{E}_y$ and $\pm\mathbf{E}_z$) field directions.

In particular, we seek to explain and quantify the origins of torsions of the $\{\boldsymbol{p}_\sigma, \boldsymbol{p'}_\sigma\}$ path-packets, associated with the Li_2 bond, that occurred when the Li_2 bond was stretched; these were previously only observed [1]. This will be undertaken by quantifying the metallic character and topological stability of the bond critical points (*BCP*s) and non-nuclear attractors (*NNA*s). Understanding of the topological stability involves tracking the creation and/or annihilation of the *BCP*s and *NNA*s. The values of the **E**-field used will be large enough to rupture the neutral Li_2 bond, i.e. to separate the two Li nuclei. The **E**-field will be applied to the symmetry inequivalent directions: parallel ($\pm\mathbf{E}_x$) and perpendicular ($\pm\mathbf{E}_y$) to the bond-path. We will compare the effect of the $\pm\mathbf{E}_x$ field with previously unpublished results from the Li_2 subject to the bond-stretching distortion, up to 12 a.u., where due to the axial symmetry the ellipticity ε remained zero along the entire bond-path. Therefore, in this investigation we will use the ellipticity $\varepsilon_{\sigma H}$ of the stress tensor $\boldsymbol{\sigma}(\mathbf{r})$ to scale the $\mathbb{B}_\sigma$ within the Hessian of $\rho(\mathbf{r})$ partitioning, which is able to detect changes in symmetry [17], [18]. This is due to the mismatch in positions of $-\boldsymbol{\nabla}\cdot\boldsymbol{\sigma}(\mathbf{r}) = 0$ for the stress tensor $\boldsymbol{\sigma}(\mathbf{r})$ calculated on the Hessian of $\rho(\mathbf{r})$ partitioning.

2. Theoretical Background and Computational Details

Scalar QTAIM, critical points, metallicity $\xi(\mathbf{r_b})$ *and the total local energy density* $H(\boldsymbol{r_b})$

The four types of QTAIM critical points are labeled using the notation (R, ω), where R is the rank of the Hessian matrix, i.e., the number of distinct non-zero eigenvalues, and ω is the signature (the algebraic sum of the signs of the eigenvalues); the (3, -3) [nuclear critical point (*NCP*), a local maximum], (3, -1) and (3, 1) [saddle points, referred to as bond critical points (*BCPs*) and ring critical points (*RCPs*), respectively] and (3, 3) [the cage critical points (*CCPs*)]. Another category of (3, -3) local maximum are non-nuclear attractors (*NNA*), which will be considered in this investigation. Additional background on QTAIM and the stress tensor $\boldsymbol{\sigma}(\mathbf{r})$ are provided in the **Supplementary Materials S1**.

The earlier observation for a tendency of $\rho(\mathbf{r})$ to remain at a closed-shell *BCP* rather than moving towards the atomic basins, which resulted in lower positive values of the Laplacian $\nabla^2\rho(\mathbf{r_b})$, where $\mathbf{r_b}$ indicates the position of the *BCP*, led directly to the concept of metallicity $\xi(\mathbf{r_b})$. The Laplacian $\nabla^2\rho(\mathbf{r_b})$ for a closed-shell *BCP* and

a shared-shell *BCP* is always positive and negative, respectively. This relative tendency for the charge to remain at or move away from a closed-shell *BCP* is defined as the metallicity $\xi(\mathbf{r_b})$:

$$\xi(\mathbf{r_b}) = \rho(\mathbf{r}_b)/\nabla^2\rho(\mathbf{r}_b) \geq 1 \text{ for } \quad \nabla^2\rho(\mathbf{r}_b) \quad > 0 \qquad \textbf{(1)}$$

Values of the metallicity $\xi(\mathbf{r_b}) \leq 1$ from equation **(1)** for closed-shell *BCP*s correspond to non-metallic or insulating *BCP*s. We earlier examined the metallicity $\xi(\mathbf{r_b})$ for very high pressure ice X [19] and intra-molecular proton transfer [20]. Values of the metallicity $\xi(\mathbf{r_b})$ for a wide range of elements and compounds [21] were examined and it was discovered that $\xi(\mathbf{r}_b)$ relates inversely to "nearsightedness" of the first-order density matrix and is suitable for closed-shell systems [22]. Note the concept of metallicity $\xi(\mathbf{r}_b)$ relates to the relative delocalization of the total electronic charge density $\rho(\mathbf{r}_b)$ [22]. The metallicity $\xi(\mathbf{r}_b)$ will be calculated on a *BCP* by *BCP* basis to enable the understanding of local changes to $\xi(\mathbf{r}_b)$ along the Li1-L2 bond-path i.e. the metallicity $\xi(\mathbf{r}_b)$ will not be summed.

A property associated with *BCP*s possessing metallicity $\xi(\mathbf{r_b})$ is that for high values of the metallicity $\xi(\mathbf{r}_b) > 1$, the total local energy density $H(\mathbf{r_b}) < 0$ for closed-shell *BCP* interactions. The total local energy density $H(\mathbf{r_b})$ is defined as:

$$H(\mathbf{r_b}) = G(\mathbf{r_b}) + V(\mathbf{r_b}) \qquad \textbf{(2)}$$

Where $G(\mathbf{r_b})$ and $V(\mathbf{r_b})$ correspond to the local kinetic energy density and the potential energy density, respectively. A previous QTAIM investigation into unusually strong hydrogen bonding found that hydrogen-bond *BCP*s with values $H(\mathbf{r_b}) < 0$, possess a degree of covalent character [23], [24].

The NG-QTAIM vector-based interpretation of the chemical bond

The bond-path framework set $\mathbb{B}_{\boldsymbol{\sigma}}$ is the NG-QTAIM interpretation of the chemical bond using the stress tensor $\boldsymbol{\sigma}(\mathbf{r})$ on the Hessian of $\rho(\mathbf{r})$ bond-path $\boldsymbol{r}$ (black-line) molecular graph, see equation **(3)** and **Figure 1**. Note, the orthogonal triad of stress tensor eigenvectors $\{\underline{\mathbf{e}}_{1\sigma}, \underline{\mathbf{e}}_{2\sigma}, \underline{\mathbf{e}}_{3\sigma}\}$ and Hessian of $\rho(\mathbf{r})$ eigenvectors $\{\underline{\mathbf{e}}_1, \underline{\mathbf{e}}_2, \underline{\mathbf{e}}_{3\sigma}\}$ are referred to as bond-path frameworks.

Bader's definition [3], [25] of the stress tensor $\boldsymbol{\sigma}(\mathbf{r})$ is used in this work as it has been successfully used before to provide physical insight into low frequency vibrational modes associated with internal molecular rearrangement [26]–[28] and is directly related to the Ehrenfest force by the virial theorem. The usual criterion for topologically stable *BCP*s is two negative eigenvalues and one positive eigenvalue directed perpendicular and parallel to the bond-path respectively. For topologically unstable *BCP*s however, there may be three

negative eigenvalues when the stress tensor $\boldsymbol{\sigma}(\mathbf{r})$ is used [18]. The stress tensor $\boldsymbol{\sigma}(\mathbf{r})$ ellipticity $\varepsilon_{\sigma H}$ is used as a scaling factor in the construction of the $\{\boldsymbol{p}_\sigma, \boldsymbol{p'}_\sigma\}$ path-packets in equation **(3)**, due to how $\boldsymbol{r}$ is constructed from ($\underline{\mathbf{e}}_3$) using the Hessian of $\rho(\mathbf{r})$:

$$\boldsymbol{p}_\sigma = \boldsymbol{r}_i + \varepsilon_{\sigma Hi}\underline{\mathbf{e}}_{2\sigma,i},\ \boldsymbol{p'}_\sigma = \boldsymbol{r}_i - \varepsilon_{\sigma Hi}\underline{\mathbf{e}}_{2\sigma,i} \qquad \textbf{(3)}$$

'Path-packet' refers to the orbital-like packet shapes that the pair of $\boldsymbol{p}_\sigma, \boldsymbol{p'}_\sigma$ paths form along the bond-path ($\boldsymbol{r}$) that will be on a Hessian of $\rho(\mathbf{r})$ molecular graph, but has earlier been superimposed onto an Ehrenfest Force $\mathbf{F(r)}$ molecular graph [1]. The $\{\boldsymbol{p}_\sigma, \boldsymbol{p'}_\sigma\}$ path-packets will be used to quantify the resistance to the applied electric-field ($\pm\mathbf{E}_x$) and ($\pm\mathbf{E}_y$) due to the $\{\boldsymbol{p}_\sigma, \boldsymbol{p'}_\sigma\}$ being constructed from $\underline{\mathbf{e}}_{2\sigma}$, the least preferred direction of electronic charge density motion $\rho(\mathbf{r})$ for the stress tensor $\boldsymbol{\sigma}(\mathbf{r})$.

Computational Details

The molecular structure was optimized with 'verytight' convergence criteria within Gaussian 09 v.E.01 [29] using the CAM-B3LYP [30]/ANO-RCC [31], [32] DFT functional and basis set. We chose this theory level to enable comparison with results, in particular unpublished metallicity $\xi(\mathbf{r}_b)$ values, from our previous investigation on the neutral Li_2 cluster [1]. Gaussian's 'superfine' DFT integration grid was used for all calculations, with an accuracy setting of 10^{-14} for the two-electron integrals. Geometry-optimization and single-point SCF calculations were performed with the aforementioned DFT settings, with the convergence criteria of $< 10^{-12}$ RMS change in the density matrix and $< 10^{-10}$ maximum change in the density matrix, with a range of external electric field values applied. These calculations yielded the wavefunctions needed for QTAIM and NG-QTAIM analysis. Calculations of the molecular graphs and critical point properties were performed using AIMAll [33], and NG-QTAIM calculations and visualization were performed using our QuantVec [34] code; the 'topviz' visualization component of QuantVec being based on the Mayavi [35] toolkit.

3. Results and Discussions

3.1 The Torsion of the Bond-Path Framework Set $\mathbb{B}_\sigma$, Metallicity $\xi(\mathbf{r}_b)$ and BCP-NNA Separations

Inspection of the Hessian of $\rho(\mathbf{r})$ bond-path framework sets $\mathbb{B}$ reveal $\{\boldsymbol{p},\boldsymbol{p'}\}$ and $\{\boldsymbol{q},\boldsymbol{q'}\}$ path-packets that are featureless as a consequence of the application of the electric fields $\pm\mathbf{E}_x$ and ($\pm\mathbf{E}_y = \pm\mathbf{E}_z$). These featureless Hessian of $\rho(\mathbf{r})$ path-packets do not enable the investigation of the origins of the bond-path torsion previously

observed [1] for the $\pm\mathbf{E}_x$-field due to the complete absence of ellipticity ε, see **Scheme 1** and the **Supplementary Materials S2**. The stress tensor $\mathbb{B}_\sigma$ will therefore be used to track the effect of the applied $\pm\mathbf{E}_x$ and $\pm\mathbf{E}_y$ scaled with the Hessian of $\rho(\mathbf{r})$ version of the stress tensor $\boldsymbol{\sigma}(\mathbf{r})$ ellipticity $\varepsilon_{\sigma H} = |\lambda_{1\sigma}|/|\lambda_{2\sigma}| - 1$, which is not featureless along the bond-path, see the **Supplementary Materials S3**.

The stress tensor $\{\boldsymbol{p}_\sigma, \boldsymbol{p'}_\sigma\}$ path-packet forms a single envelope around all three critical points, *BCP*1, *NNA*3 and *BCP*2, for the **E**-field = 0, see **Figure 1**. The stress tensor $\underline{\mathbf{e}}_{2\sigma}$ eigenvector was used for displaying the $\{\boldsymbol{p}_\sigma,\boldsymbol{p'}_\sigma\}$ path-packets because once the ±**E**-field was applied, it remained aligned exactly with one of the Cartesian *y* or *z* directions for both the $\pm\mathbf{E}_x$ and $\pm\mathbf{E}_y$. Conversely, the stress tensor $\underline{\mathbf{e}}_{1\sigma}$ eigenvector was misaligned with any of the Cartesian axes for $\pm\mathbf{E}_y$ due to fractional rotation of the bond-path framework $\{\underline{\mathbf{e}}_{1\sigma}, \underline{\mathbf{e}}_{2\sigma}, \underline{\mathbf{e}}_{3\sigma}\}$, see the **Supplementary Materials S4**.

Examination of the Cartesian *x*, *y*, *z* axes of the stress tensor $\boldsymbol{\sigma}(\mathbf{r})$ eigenvectors $\{\underline{\mathbf{e}}_{1\sigma}, \underline{\mathbf{e}}_{2\sigma}, \underline{\mathbf{e}}_{3\sigma}\}$ for the **E**-field = 0 demonstrates that the $\underline{\mathbf{e}}_{1\sigma}$ is aligned with the Cartesian *x*-axis, i.e. the bond-path, instead of the usual case of $\underline{\mathbf{e}}_{3\sigma}$ being aligned with bond-path. At **E**-field = 0 the orthogonal set of stress tensor eigenvector bond-path framework $\{\underline{\mathbf{e}}_{1\sigma}, \underline{\mathbf{e}}_{2\sigma}, \underline{\mathbf{e}}_{3\sigma}\}$ was rotated by π/2 radians relative to the Cartesian coordinate frame, compared with that of the Hessian of $\rho(\mathbf{r})$, which was aligned with the Cartesian coordinate frame. The stress tensor eigenvectors $\boldsymbol{\sigma}(\mathbf{r})$ were oriented $\{\underline{\mathbf{e}}_{1\sigma} \rightarrow \boldsymbol{x}, \underline{\mathbf{e}}_{2\sigma} \rightarrow \boldsymbol{y}, \underline{\mathbf{e}}_{3\sigma} \rightarrow \boldsymbol{z}\}$ compared with the Hessian of $\rho(\mathbf{r})\{\underline{\mathbf{e}}_1 \rightarrow \boldsymbol{y}, \underline{\mathbf{e}}_2 \rightarrow \boldsymbol{z}, \underline{\mathbf{e}}_3 \rightarrow \boldsymbol{x}\}$ where *x*, *y*, *z* correspond to the Cartesian axes where *x* is aligned with the bond-path, see **Figure 1**. The eigenvectors $\{\underline{\mathbf{e}}_1, \underline{\mathbf{e}}_2, \underline{\mathbf{e}}_3\}$ of the Hessian of $\rho(\mathbf{r})$ for **E**-field = 0 however, possess a positive λ_3 eigenvalue associated with the bond-path, where the Hessian of $\rho(\mathbf{r})$ eigenvector $\underline{\mathbf{e}}_3$ is aligned with bond-path as in most molecular graphs, see the **Supplementary Materials S5**.

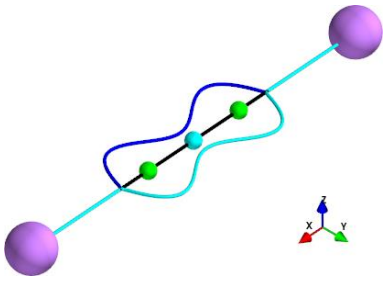

Figure 1. The neutral Li_2 lithium molecular graph displaying the stress tensor $\{\boldsymbol{p}_\sigma$(blue), $\boldsymbol{p'}_\sigma$(cyan)$\}$ path-packets on the Li1-Li2 bond-path ($\boldsymbol{r}$), for values of the electric field, **E**-field = 0, see **Scheme 1** for the $\pm\mathbf{E}_x$, $\pm\mathbf{E}_y$ and $\pm\mathbf{E}_z$ directions.

The effect on the $\{\boldsymbol{p}_\sigma,\boldsymbol{p'}_\sigma\}$ path-packets of the $\pm\mathbf{E}_x$ and $\pm\mathbf{E}_y$ electric fields, with magnitudes up to $\pm100.0\text{x}10^{-4}$ a.u., are presented in **Figure 2** and **Figure 3**, respectively. The corresponding $\{\boldsymbol{p}_\sigma,\boldsymbol{p'}_\sigma\}$ path-packets for the largest $\pm\mathbf{E}_x$ and $\pm\mathbf{E}_y$ electric fields before bond-path rupture are presented in **Figure 4** and **Figure 5** respectively.

Additional views in the *x*-*z* plane of the $\{\boldsymbol{p}_\sigma,\boldsymbol{p'}_\sigma\}$ path-packets subjected to the $\pm\mathbf{E}_x$ and $\pm\mathbf{E}_y$ electric fields are provided in the **Supplementary Materials S6**.

The stress tensor $\{\boldsymbol{p}_\sigma,\boldsymbol{p'}_\sigma\}$ path-packets subject to the $\pm\mathbf{E}_x$-field for $\mathbf{E} = 0$ and some low field values, surround both *BCP*s in a single envelope, which separated into two envelopes as the magnitude of the $\pm\mathbf{E}_x$-field increased. These envelopes surrounding the *BCP*s persisted in the vicinity of the *NNA* after the *BCP* had ruptured. A single envelope persisted with application of the $\pm\mathbf{E}_y$-field, until the bond had ruptured.

For all values of $\pm\mathbf{E}_x$-field the $\underline{\mathbf{e}}_3$ eigenvector of the Hessian of $\rho(\mathbf{r})$ remained aligned with the bond-path, whereas the Cartesian directions of the $\underline{\mathbf{e}}_1$ and $\underline{\mathbf{e}}_2$ swap, due to the consistently zero ellipticity ε values rendering $\underline{\mathbf{e}}_1$ and $\underline{\mathbf{e}}_2$ equivalent. The eigenvectors of the Hessian of $\rho(\mathbf{r})$ were initially in a topologically stable configuration, but were destabilized by the application of the $\pm\mathbf{E}_y$-field and reoriented to a stable configuration for the highest **E**-field values before bond rupture. There is continuous rotation of the Hessian of $\rho(\mathbf{r})$ bond-path framework with increase in $\pm\mathbf{E}_y$-field. This results in the $\underline{\mathbf{e}}_3$ eigenvectors of *BCP*1 and *BCP*2 at $\pm\mathbf{E}_y = \pm 160.0\text{x}10^{-4}$ a.u. of the Hessian of $\rho(\mathbf{r})$ bond-path framework, which was initially orientated along the *z*-axis, rotating to realign with the *x*-axis. This rotation of the Hessian of $\rho(\mathbf{r})$ bond-path framework from initial alignment of the $\underline{\mathbf{e}}_3$ eigenvector with the *x*-axis to alignment with the *z*-axis coincides with the maximum value of the metallicity $\xi(\mathbf{r}_b)$ for the $\pm\mathbf{E}_y$-field, **Figure 7(b)** and the **Supplementary Materials S7**. All instances of metallic character, i.e. $\xi(\mathbf{r}_b) \geq 1$, also possess small negative values of the total local energy density $H(\mathbf{r}_b)$. Finally, just before bond rupture, the Hessian of $\rho(\mathbf{r})$ bond-path framework rotates back to the initial configuration along the *x*-axis.

Significant differences in the effect on the path-packet morphology and orientation are clearly seen in the stress tensor $\{\boldsymbol{p}_\sigma,\boldsymbol{p'}_\sigma\}$ for the $+\mathbf{E}_x$ and $-\mathbf{E}_x$ directions of the **E**-field for both the lower and higher values of $\pm\mathbf{E}_x$, see **Figure 2** and **Figure 4**, respectively. There are also differences in the $\{\boldsymbol{p}_\sigma,\boldsymbol{p'}_\sigma\}$ path-packet morphology and orientation as a function of the magnitude of the $\pm\mathbf{E}_x$-field. The origins of these differences in the $\{\boldsymbol{p}_\sigma,\boldsymbol{p'}_\sigma\}$ path-packet morphologies are explained by the changing orientation of the stress tensor $\boldsymbol{\sigma}(\mathbf{r})$ bond-path framework constructed from the orthogonal set $\{\underline{\mathbf{e}}_{1\sigma}, \underline{\mathbf{e}}_{2\sigma}, \underline{\mathbf{e}}_{3\sigma}\}$. Significant differences in the $\{\boldsymbol{p}_\sigma,\boldsymbol{p'}_\sigma\}$ are not apparent for the corresponding $+\mathbf{E}_y$ and $-\mathbf{E}_y$ directions of the **E**-field; however the bond-paths for higher $+\mathbf{E}_y$ and $-\mathbf{E}_y$ values bend significantly along the $+y$ and $-y$ Cartesian directions, respectively, see **Figure 3** and **Figure 5**.

An *NNA-NNA BCP* exists for values of the $\pm\mathbf{E}_y$-field = $\pm 255.0\text{x}10^{-4}$ a.u. to $\pm 269.0\text{x}10^{-4}$ a.u., which is a unique topological feature that has an associated *non-rotated* bond-path framework $\{\underline{\mathbf{e}}_{1\sigma}, \underline{\mathbf{e}}_{2\sigma}, \underline{\mathbf{e}}_{3\sigma}\}$, i.e. $\underline{\mathbf{e}}_{3\sigma}$ is aligned with the bond-path and the *x*-axis, see **Figure 5(c)**. *NNA*s were absent and only a single *BCP* remained for the Li_2 molecular graphs just before the rupture of the bond-path for both the $\pm\mathbf{E}_x$ and $\pm\mathbf{E}_y$ fields.

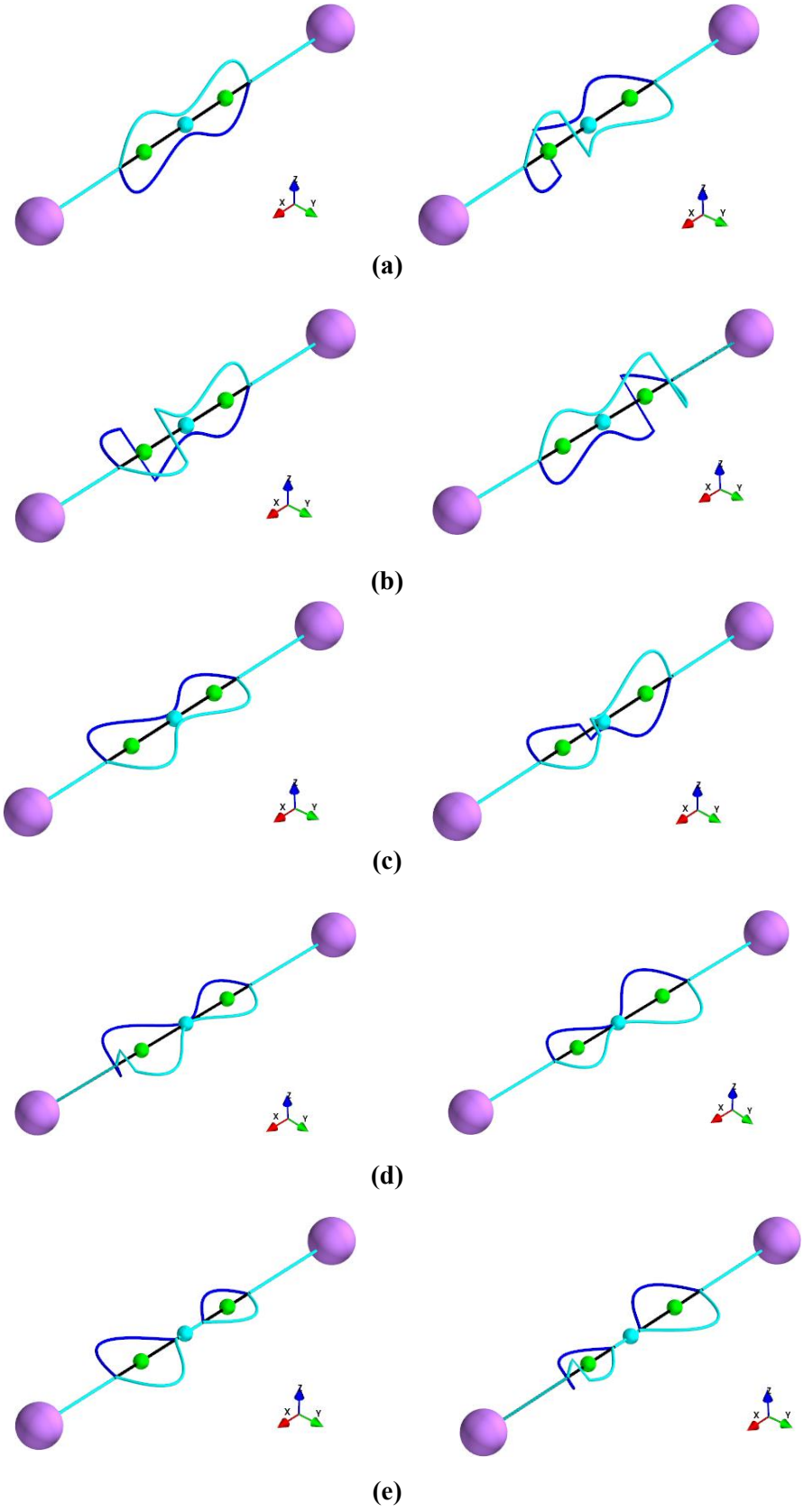

Figure 2. The $\{p_\sigma,p'_\sigma\}$ stress tensor path-packets for values of the electric field, for (+$\mathbf{E}_x$) are presented in the left and right (-$\mathbf{E}_x$) panels respectively. Values of the $\mathbf{E}_x$-field (in a.u.) = $\pm 20.0\text{x}10^{-4}$, $\pm 40.0\text{x}10^{-4}$, $\pm 60.0\text{x}10^{-4}$, $\pm 80.0\text{x}10^{-4}$, $\pm 100.0\text{x}10^{-4}$ correspond to sub-figures **(a-e)**, respectively. See **Figure 1** for the $\mathbf{E} = 0$ $\{p_\sigma,p'_\sigma\}$ path-packets and **Scheme 1** for the **E**-field directions.

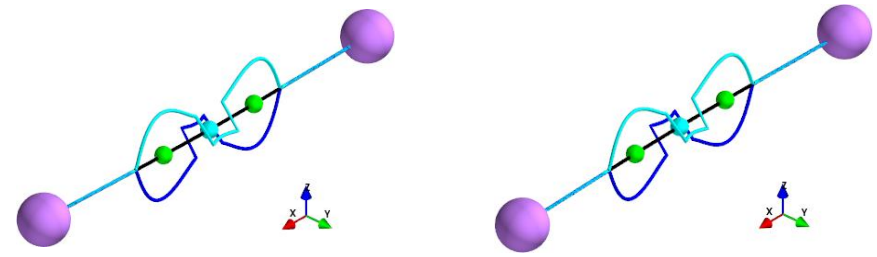

(a)

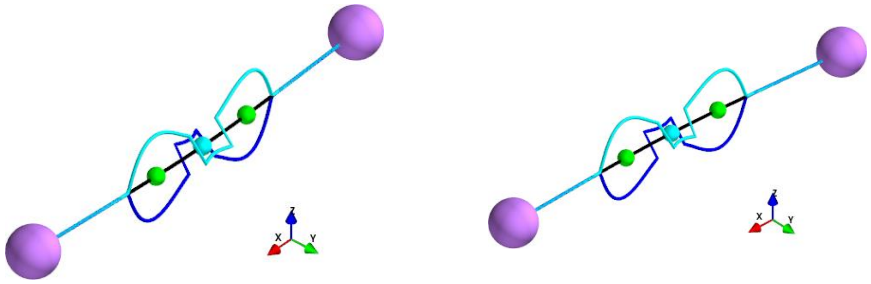

(b)

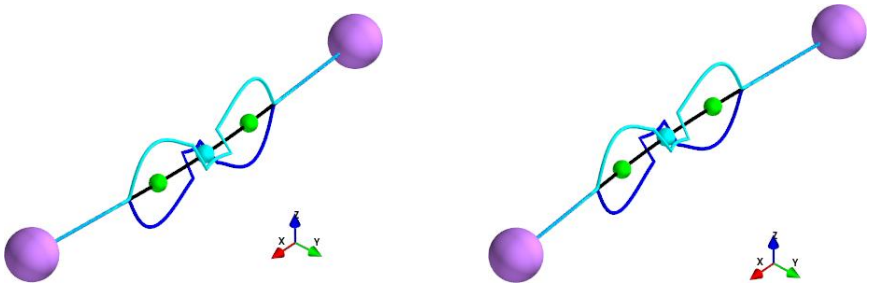

(c)

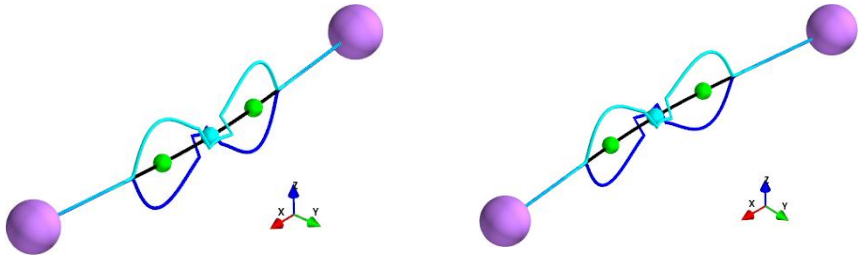

(d)

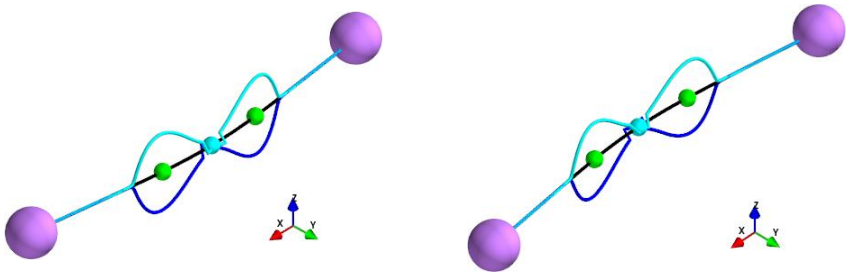

(e)

Figure 3. The stress tensor $\{p_\sigma, p'_\sigma\}$ path-packets for values of ($+\mathbf{E}_y$) are presented in the left and right ($-\mathbf{E}_y$) panels respectively, for values of the $\pm\mathbf{E}_y$-field (in a.u.) = $\pm 20.0\text{x}10^{-4}$, $\pm 40.0\text{x}10^{-4}$, $\pm 60.0\text{x}10^{-4}$, $\pm 80.0\text{x}10^{-4}$, $\pm 100.0\text{x}10^{-4}$ correspond to sub-figures **(a-e)**, respectively. See **Figure 2** for further details.

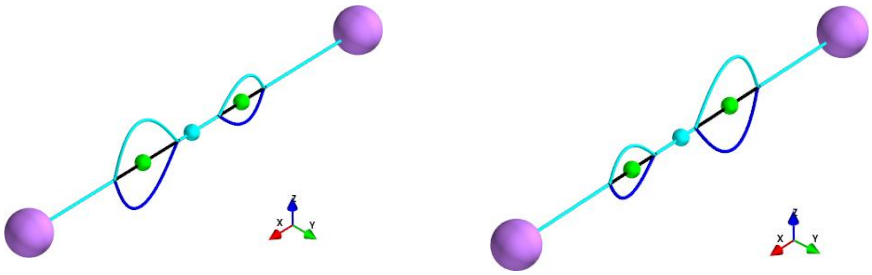

(a)

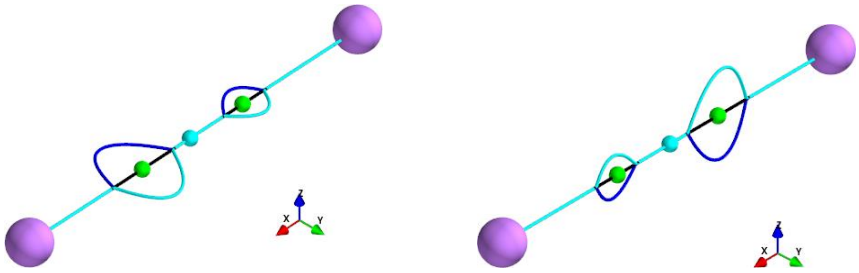

(b)

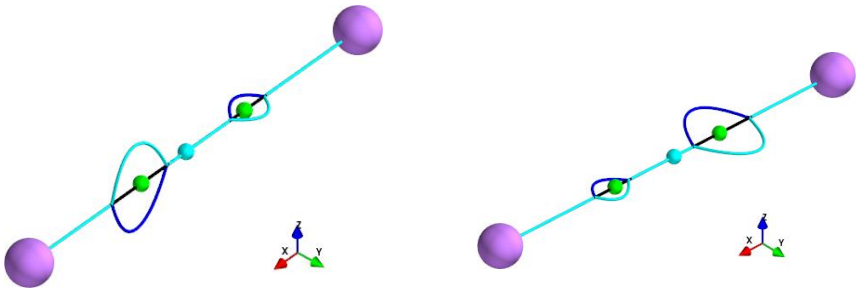

(c)

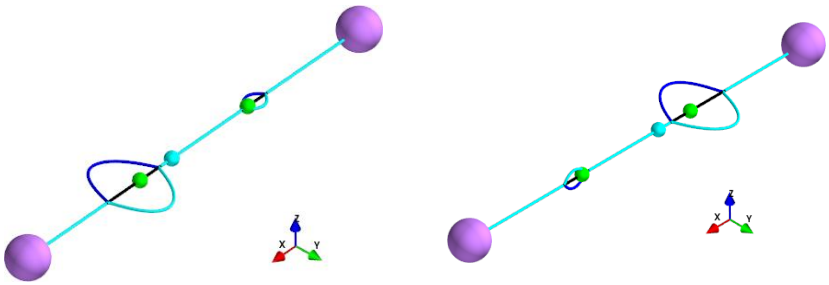

(d)

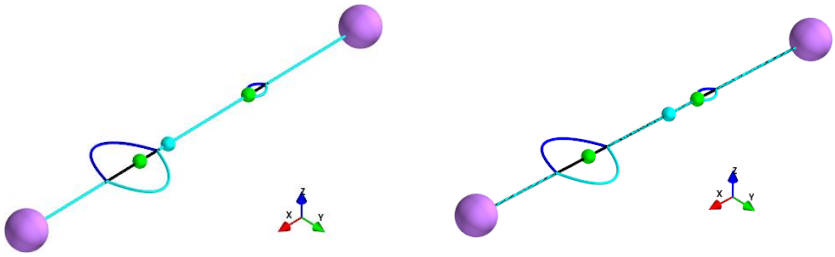

(e)

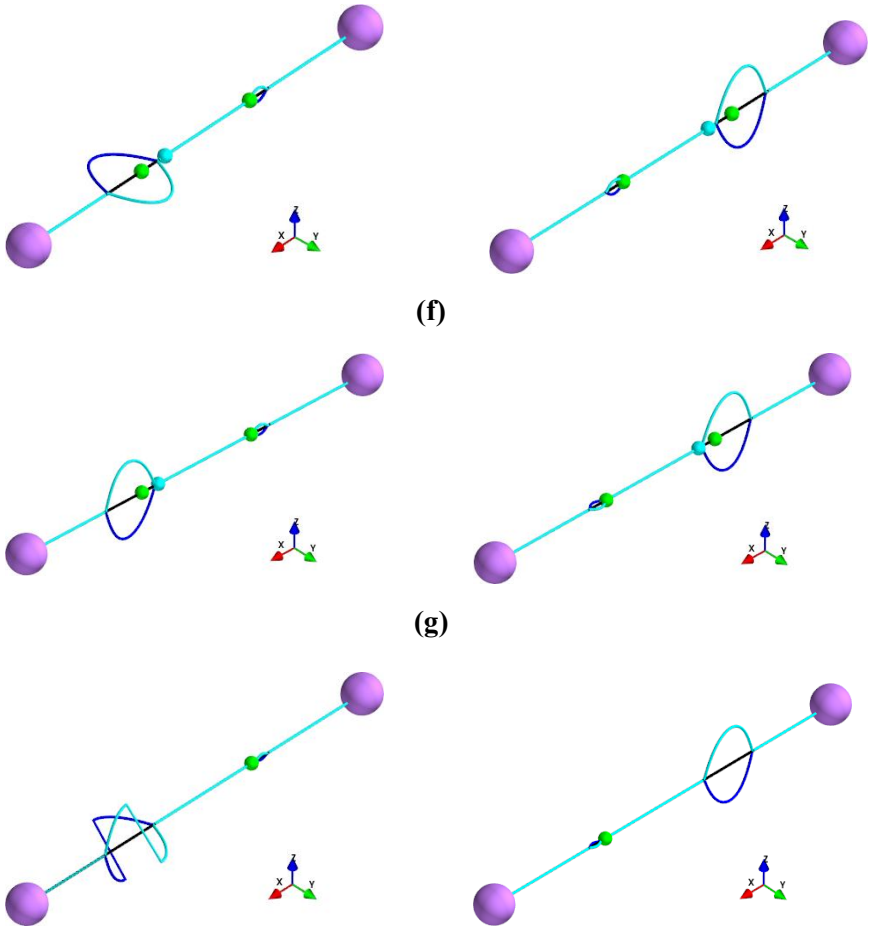

(f)

(g)

(h)

Figure 4. The stress tensor $\{p_\sigma, p'_\sigma\}$ path-packets for values of (+$\mathbf{E}_x$) are presented in the left and right (-$\mathbf{E}_x$) panels respectively. the values of the electric field, ±$\mathbf{E}_x$-field (in a.u.) = ±110.0x10^{-4}, ±120.0x10^{-4}, ±130.0x10^{-4}, ±140.0x10^{-4}, ±141.0x10^{-4}, ±142.0x10^{-4}, ±143.0x10^{-4}, ±144.0x10^{-4} correspond to sub-figures **(a-h)**, respectively. See **Figure 2** for further details.

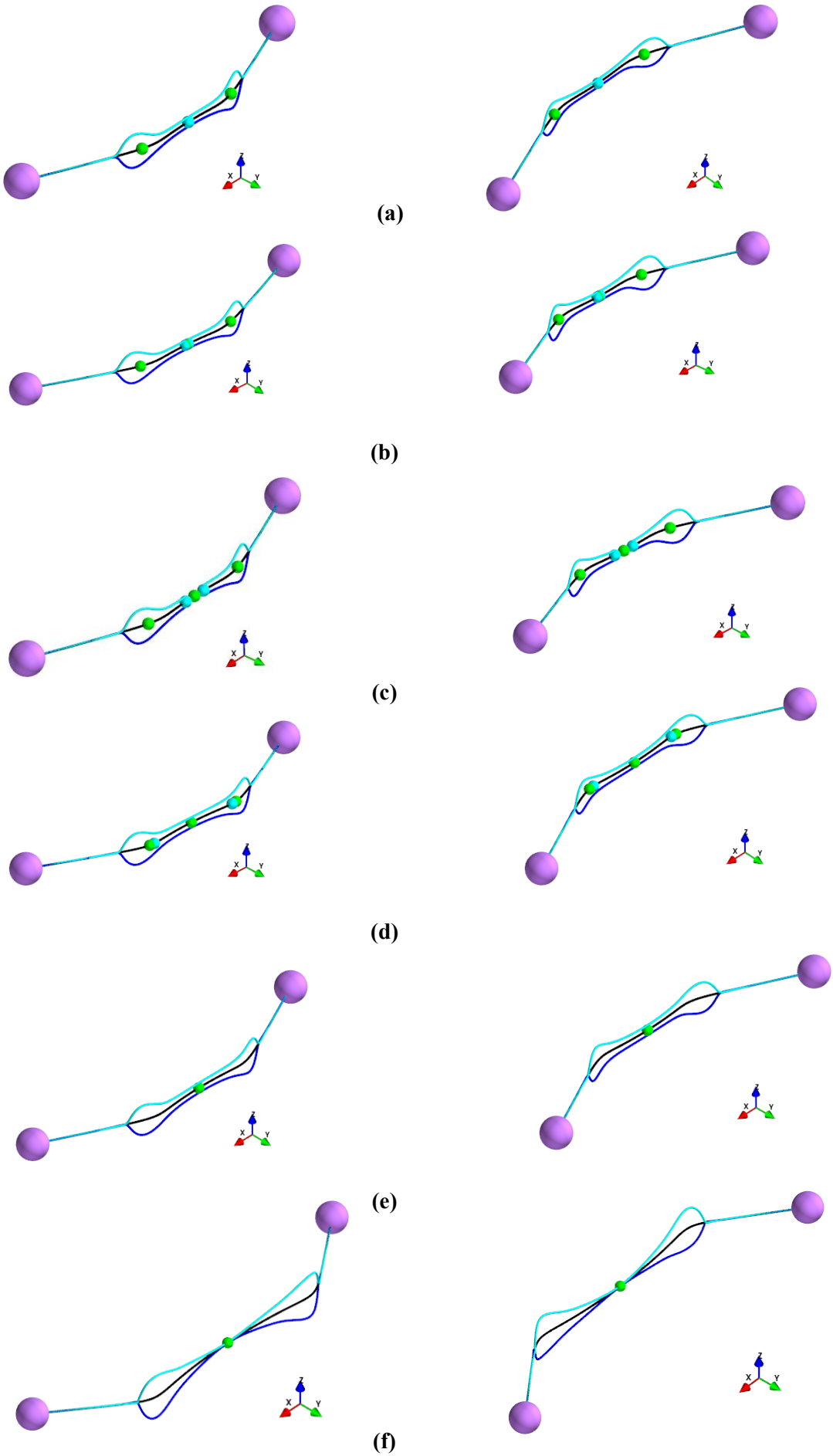

Figure 5. The stress tensor $\{p_\sigma, p'_\sigma\}$ path-packets for (+$\mathbf{E}_y$) are presented in the left and right (-$\mathbf{E}_y$) panel respectively. Values for ±$\mathbf{E}_y$-field (in a.u.) = ±255.0x10^{-4}, ±256.0x10^{-4}, ±257.0x10^{-4}, ±269.0x10^{-4}, ±270.0x10^{-4} and ±294.0x10^{-4} correspond to sub-figures **(a-f),** respectively, see **Figure 2** for further details.

The *NNA* is generally more mobile, i.e. possesses larger Li-*CP* separations, than the *BCP*s along the bond-path for both the ±**E**$_x$-field and ±**E**$_y$-fields, see **Figure 6**. Comparing the effect of the ±**E**$_x$-field and ±**E**$_y$-field, the mobility of the *NNA* is significantly higher, although the *BCP*s possess generally similar mobility for both **E**-field directions. These differences in the mobility of the *NNA* for the ±**E**$_x$-field and ±**E**$_y$-field direction may account for the corresponding differences in the *BCP* metallicity $\xi(\mathbf{r}_b)$, see **Figure 7**. The metallicity $\xi(\mathbf{r}_b)$ attains much higher values for the ±**E**$_x$-field compared with the ±**E**$_y$-field direction, where *BCP*1 and *BCP*2 possess mirror image values of $\xi(\mathbf{r}_b)$ for the ±**E**$_x$-field direction.

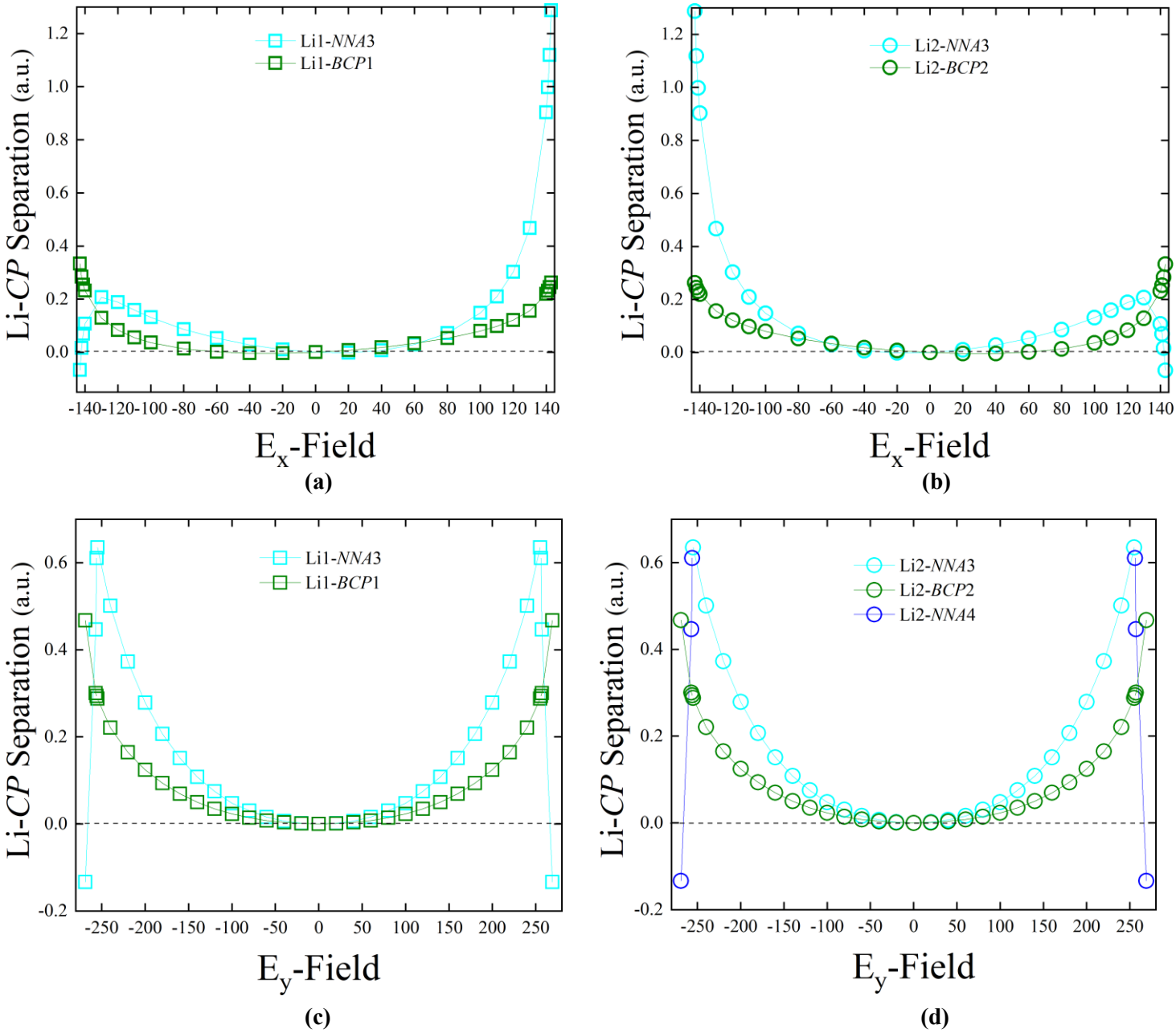

Figure 6. Plots of the variation of the Li-*CP* separation with ±**E**$_x$ are presented in sub-figures **(a)** and **(b)**. Critical points (*CP*s) correspond to the bond critical points (*BCP*s) and non-nuclear attractors (*NNAs*). The *NNA*3 and *NNA*4 are shown surrounding the central *BCP* on the Li_2 molecular graph in **Figure 5(c)**, also see **Scheme 1**. The corresponding plots for the variations of ±**E**$_y$ are presented in sub-figures **(c)** and **(d)**.

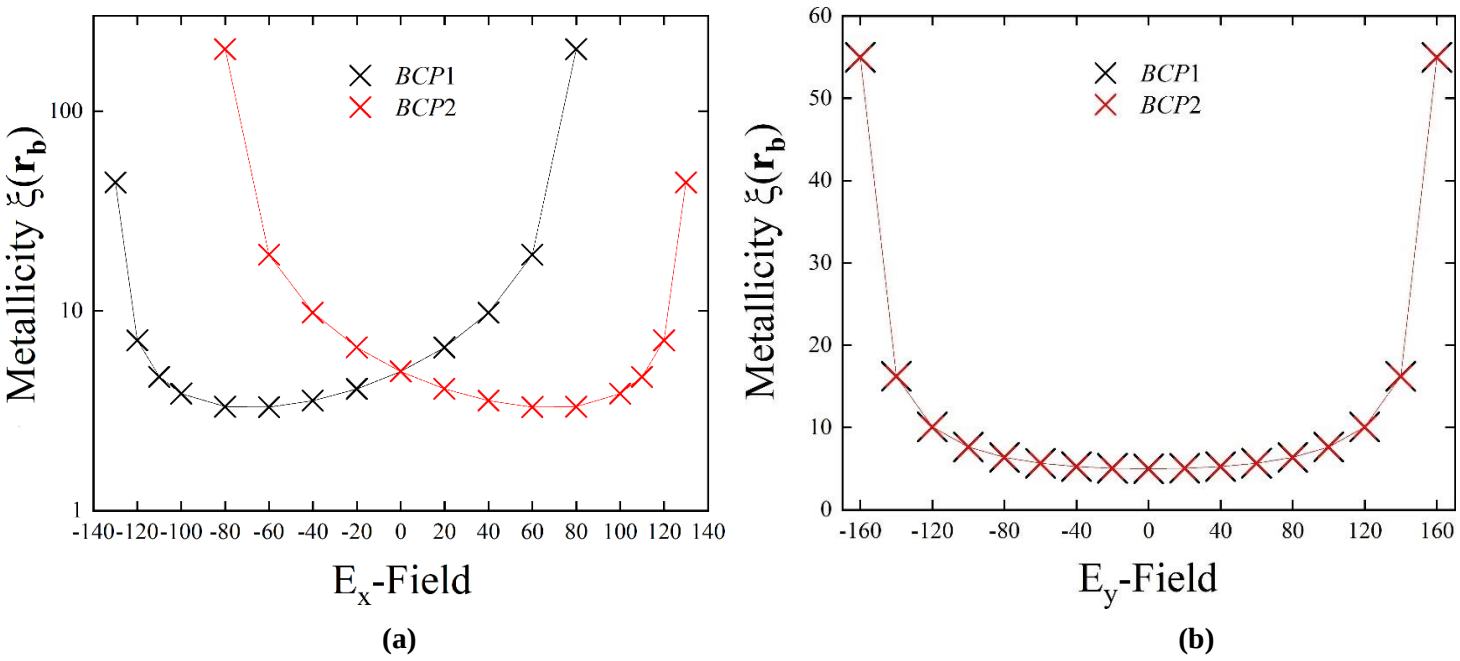

Figure 7. The variation of *BCP* metallicity $\xi(\mathbf{r}_b)$ with the $\pm\mathbf{E}_x$-field and $\pm\mathbf{E}_y$-field of the Li_2 molecular graph are presented in sub-figures **(a-b)**, respectively. a.u. units are used throughout. Notice the $\log_{10}$ scale for sub-figure **(a)**, see **Scheme 1** for further details.

Comparison can be made with previously overlooked and unpublished results from our earlier investigation into stretching distortions of neutral Li_2, in the absence of an **E**-field, with the effects of the $\pm\mathbf{E}_x$-field. The Hessian of $\rho(\mathbf{r})$ results, including $\rho(\mathbf{r}_b)$, Laplacian $\nabla^2\rho(\mathbf{r}_b)$ and *BCP* metallicity $\xi(\mathbf{r}_b)$ corresponding to the neutral Li_2 stretching distortions, were not previously published; only the geometric bond-length (GBL) was previously published [1].

For a $\pm\mathbf{E}_x$-field value of $\pm144.0\text{x}10^{-4}$ a.u. the *NNA* is annihilated and the BPL is 6.406 a.u. The Li_2 bond-path ruptures for a value of the $\pm\mathbf{E}_x$-field = $\pm145.0\text{x}10^{-4}$ a.u. The critical points are not positioned symmetrically for all values of the applied $\pm\mathbf{E}_x$-field, see **Figure 6(a-b)** where it can be seen that the *NNA*s are significantly more mobile on the bond-path than the *BCP*s, see the **Supplementary Materials S8**. Significant values of the metallicity $\xi(\mathbf{r}_b)$ occur for a wide range of $\pm\mathbf{E}_x$-field values.

In comparison, the neutral Li_2 subjected to the stretching distortion exists until the bond-path length (BPL = GBL) is 12.1 a.u., although values of the Laplacian $\nabla^2\rho(\mathbf{r}_b)$ are insignificant beyond 10.1 a.u. and the *NNA* is annihilated when the BPL is 7.1 a.u. Additional new results for the stretched neutral Li_2 include the eigenvectors $\{\underline{\mathbf{e}}_1, \underline{\mathbf{e}}_2, \underline{\mathbf{e}}_3\}$ of the Hessian of $\rho(\mathbf{r})$ and the stress tensor $\boldsymbol{\sigma}(\mathbf{r})$ eigenvectors $\{\underline{\mathbf{e}}_{1\sigma}, \underline{\mathbf{e}}_{2\sigma}, \underline{\mathbf{e}}_{3\sigma}\}$, see the **Supplementary Materials S9**. For all values of the stretching distortion the critical points are positioned symmetrically about the geometric centre of the Li1-Li2 bond-path and the *NNA* remains fixed at the centre of the bond-path for all stretching distortions. A significant value of the metallicity $\xi(\mathbf{r}_b)$, i.e. $\xi(\mathbf{r}_b) = 40.1$ a.u., only occurs for a Li1-Li2 separation of 6.1 a.u., which may be explained by the lack of mobility of the *NNA* for the stretching distortions. The stress tensor eigenvalue $\lambda_{3\sigma}$ for the stretching distortion was negative up to

an extension of 6.1 a.u., where there were two *BCP*s. All longer extensions were associated with a single *BCP* and a positive value of stress tensor eigenvalue $\lambda_{3\sigma}$.

4. Conclusions

In this investigation we set out to better understand the underlying causes, firstly of torsion of the $\{\boldsymbol{p}_\sigma,\boldsymbol{p'}_\sigma\}$ path-packets, and secondly changes to the critical point topology of the molecular graph of neutral Li_2 as a consequence of applying an electric ($\pm\mathbf{E}$)-field, both parallel ($\pm\mathbf{E}_x$) and perpendicular ($\pm\mathbf{E}_y$) to the bond-path. We have used NG-QTAIM with the stress tensor $\boldsymbol{\sigma}(\mathbf{r})$ to understand the directional properties associated with the eigenvectors of scalar QTAIM and the Hessian of $\rho(\mathbf{r})$. In addition, the stress tensor ellipticity $\varepsilon_{\sigma H}$ was non-zero for the application of the $\pm\mathbf{E}$-field, in contrast with the Hessian of $\rho(\mathbf{r})$, which had two associated negative *BCP*s.

The scalar QTAIM properties were used to obtain the neutral Li_2 molecular graph, *BCP*s, *NNA*s etc. and metallicity $\xi(\mathbf{r}_b)$ using the Hessian of $\rho(\mathbf{r})$ partitioning, since the stress tensor $\boldsymbol{\sigma}(\mathbf{r})$ lacks an associated scalar- or vector-field partitioning scheme. The rotation of stress tensor bond-path framework $\{\underline{\mathbf{e}}_{1\sigma}, \underline{\mathbf{e}}_{2\sigma}, \underline{\mathbf{e}}_{3\sigma}\}$ due to the application of both the $\pm\mathbf{E}_x$ and $\pm\mathbf{E}_y$-field occurred despite the absence of structural asymmetry induced by the $\pm\mathbf{E}_x$-field. This finding indicates that the stress tensor $\boldsymbol{\sigma}(\mathbf{r})$ eigenvectors can be used to detect the presence of the bond-path framework $\{\underline{\mathbf{e}}_{1\sigma}, \underline{\mathbf{e}}_{2\sigma}, \underline{\mathbf{e}}_{3\sigma}\}$ rotation, i.e. topological instability, regardless of the induced bond-path asymmetry caused by bond-path bending. This topological instability can be explained by the presence of three negative *BCP* stress tensor eigenvalues, which is characteristic of topologically unstable *BCP*s [18].

The Hessian of $\rho(\mathbf{r})$ bond-path framework $\{\underline{\mathbf{e}}_1, \underline{\mathbf{e}}_2, \underline{\mathbf{e}}_3\}$ did not rotate in response to the application of the $\pm\mathbf{E}_x$-field, due to the lack of bond bending, i.e. asymmetry induced by the $\pm\mathbf{E}_y$-field.

For the highest $\pm\mathbf{E}_x$-field values before bond rupture, the $\{\boldsymbol{p}_\sigma,\boldsymbol{p'}_\sigma\}$ path-packets persisted in the vicinity of the *NNA* after the *BCP* had ruptured, which is an indicator of the topologically stabilizing effect of the *NNA*. For the $\pm\mathbf{E}_y$-field a single $\{\boldsymbol{p}_\sigma,\boldsymbol{p'}_\sigma\}$ envelope with the largest extent surrounding the *NNA*s persisted until the bond ruptured, which also indicated a topologically stabilizing effect of the *NNA*.

An *NNA-NNA BCP* was uniquely present as an adaptation to the higher values of the $\pm\mathbf{E}_y$-field = $\pm 255.0 \times 10^{-4}$ a.u. to $\pm 269.0 \times 10^{-4}$ a.u., which resulted in significant neutral Li_2 *BCP* bond-path bending. This can be explained by the *NNA-NNA BCP* possessing a positive stress tensor eigenvalue $\lambda_{3\sigma}$, which is associated with topologically stable *BCP*s. The *NNA*s shifted along the bond-path more for the applied $\pm\mathbf{E}_x$-field than the $\pm\mathbf{E}_y$-field, which can explain the presence of higher values of the metallicity $\xi(\mathbf{r}_b)$ for the $\pm\mathbf{E}_x$-field compared with the $\pm\mathbf{E}_y$-field.

The overall directional effect of the applied $\pm\mathbf{E}_x$ and $\pm\mathbf{E}_y$-fields is to reorient the stress tensor $\boldsymbol{\sigma}(\mathbf{r})$ eigenvectors with increase in $\pm\mathbf{E}$-field until just before the bond rupture, where the stress tensor $\underline{\mathbf{e}}_{3\sigma}$ eigenvector is finally orientated along the bond-path with a single *BCP* and no *NNA*s. The overall scalar effect induced by the

applied $\pm\mathbf{E}_x$ and $\pm\mathbf{E}_y$-fields is to increase the values of the metallicity $\xi(\mathbf{r}_b)$ and motion of the *NNA*s along the bond-path.

Comparison of the stretching distortion of neutral Li_2 in the absence of an applied $\pm\mathbf{E}_x$-field was made. The stretching distortion resulted in the GBL being approximately twice (≈12 a.u.) that of the neutral Li_2 subject to the $\pm\mathbf{E}_x$-field (≈6 a.u.) before bond rupture. This difference could be explained by the greater motion of the *NNA*s and higher metallicity $\xi(\mathbf{r}_b)$ present for the Li_2 subjected to the $\pm\mathbf{E}_x$-field, which causes the bond to rupture at shorter lengths compared with the Li_2 stretching distortion. Our work here is consistent with the work of Terrabuio and Teodoro *et al*. since the polarization effect induced by the applied $\pm\mathbf{E}_x$-field, induced a greater stabilization, up to and including values of $\pm\mathbf{E}_x$-field = $\pm 143.0 \times 10^{-4}$ a.u., of the *NNA*s. This stabilization effect took the form of the reorientation of the stress tensor $\boldsymbol{\sigma}(\mathbf{r})$ bond-path framework $\{\underline{\mathbf{e}}_{1\sigma}, \underline{\mathbf{e}}_{2\sigma}, \underline{\mathbf{e}}_{3\sigma}\}$ and Hessian of $\rho(\mathbf{r})$ bond-path framework $\{\underline{\mathbf{e}}_1, \underline{\mathbf{e}}_2, \underline{\mathbf{e}}_3\}$

Future investigations with NG-QTAIM and lithium clusters could include charged species and manipulation of the positions and existence of the *NNA*s using linearly polarized non-ionizing ultra-fast laser irradiation. The laser irradiation would be on sufficiently fast timescales to avoid disrupting the lithium nuclei positions.

Conflict of Interests Statement

The authors have no conflict of interests to declare.

Funding: The Hunan Natural Science Foundation of China project gratefully acknowledged approval number: 2022JJ30029. The One Hundred Talents Foundation of Hunan Province is also gratefully acknowledged for the support of S.J. and S.R.K.

References

[1] A. Azizi, R. Momen, S. R. Kirk, S. Jenkins, *Phys. Chem. Chem. Phys.*, **2019**, DOI:10.1039/C9CP05066C.
[2] L. A. Terrabuio, T. Q. Teodoro, C. F. Matta, R. L. A. Haiduke, *J. Phys. Chem. A*, **2016**, DOI:10.1021/acs.jpca.5b10888.
[3] R. F. W. Bader, *J. Chem. Phys.*, **1980**, DOI:10.1063/1.440457.
[4] R. F. W. Bader, in Atoms in Molecule: A Quantum Theory, **1990**; Vol. 22.
[5] J. R. Maza, S. Jenkins, S. R. Kirk, J. S. M. Anderson, P. W. Ayers, *Phys. Chem. Chem. Phys.*, **2013**, DOI:10.1039/C3CP52687A.
[6] A. Tachibana, *J. Chem. Phys.*, **2001**, DOI:10.1063/1.1384012.
[7] A. Tachibana, *Int. J. Quantum Chem.*, **2004**, DOI:10.1002/qua.20258.
[8] A. Tachibana, *J. Mol. Model.*, **2005**, DOI:10.1007/s00894-005-0260-y.
[9] P. Szarek, Y. Sueda, A. Tachibana, *J. Chem. Phys.*, **2008**, DOI:10.1063/1.2973634.
[10] T. Xu, J. Farrell, R. Momen, A. Azizi, S. R. Kirk, S. Jenkins, D. J. Wales, *Chem. Phys. Lett.*, **2017**, DOI:10.1016/j.cplett.2016.11.028.
[11] T. Xu, J. H. Li, R. Momen, W. J. Huang, S. R. Kirk, Y. Shigeta, S. Jenkins, *J. Am. Chem. Soc.*, **2019**, DOI:10.1021/jacs.9b00823.

[12] P. Yang, T. Xu, R. Momen, A. Azizi, S. R. Kirk, S. Jenkins, *Int. J. Quantum Chem.*, **2018**, DOI:10.1002/qua.25565.
[13] P. Szarek, A. Tachibana, *J. Mol. Model.*, **2007**, DOI:10.1007/s00894-007-0215-6.
[14] A. Azizi, R. Momen, T. Xu, S. R. Kirk, S. Jenkins, *Phys. Chem. Chem. Phys.*, **2018**, DOI:10.1039/C8CP05214J.
[15] S. R. Kirk, S. Jenkins, *WIREs Comput. Mol. Sci.*, **2022**, DOI:10.1002/wcms.1611.
[16] H. Nakatsuji, *J. Am. Chem. Soc.*, **1974**, DOI:10.1021/ja00808a004.
[17] T. Xu, S. R. Kirk, S. Jenkins, *Chem. Phys. Lett.*, **2020**, DOI:10.1016/j.cplett.2019.136907.
[18] S. Jenkins, J. R. Maza, T. Xu, D. Jiajun, S. R. Kirk, *Int. J. Quantum Chem.*, **2015**, DOI:10.1002/qua.25006.
[19] S. Jenkins, S. R. Kirk, P. W. Ayers, Structural and chemical character of very high pressure ice phases, *Physics and Chemistry of Ice (Proceedings of 11th International Conference on the Physics and Chemistry of Ice, Bremerhaven, Germany)*. Royal Society of Chemistry, Bremerhaven, Germany, 265–272, 2006.
[20] S. Mitra, A. Chandra, P. Gashnga, S. Jenkins, S. Kirk, *J. Mol. Model.*, **2012**, DOI:10.1007/s00894-012-1408-1.
[21] S. Jenkins, P. W. Ayers, S. R. Kirk, P. Mori-Sánchez, A. Martín Pendás, *Chem. Phys. Lett.*, **2009**, DOI:10.1016/j.cplett.2009.02.018.
[22] P. W. Ayers, S. Jenkins, *Comput. Theor. Chem.*, **2015**, DOI:10.1016/j.comptc.2014.10.040.
[23] D. Cremer, E. Kraka, *Croat. Chem. Acta*, **1984**, *57*, 1259–1281.
[24] I. Rozas, I. Alkorta, J. Elguero, *J. Am. Chem. Soc.*, **2000**, DOI:10.1021/ja0017864.
[25] R. F. W. Bader, T. T. Nguyen-Dang, Quantum Theory of Atoms in Molecules–Dalton Revisited, *Advances in Quantum Chemistry*, *14*. Academic Press, New York, 63–124, 1981.
[26] A. Guevara-García, E. Echegaray, A. Toro-Labbe, S. Jenkins, S. R. Kirk, P. W. Ayers, *J. Chem. Phys.*, **2011**, DOI:10.1063/1.3599935.
[27] P. W. Ayers, S. Jenkins, *J. Chem. Phys.*, **2009**, DOI:10.1063/1.3098140.
[28] A. Guevara-García, P. W. Ayers, S. Jenkins, S. R. Kirk, E. Echegaray, A. Toro-Labbe, Electronic Stress as a Guiding Force for Chemical Bonding, *Electronic Effects in Organic Chemistry*. Springer Berlin Heidelberg, Berlin, Heidelberg, 103–124, 2014.
[29] Michael J. Frisch, G. W. Trucks, H. Bernhard Schlegel, Gustavo E. Scuseria, Michael A. Robb, James R. Cheeseman, Giovanni Scalmani, Vincenzo Barone, Benedetta Mennucci, G. A. Petersson, H. Nakatsuji, M. Caricato, Xiaosong Li, H. P. Hratchian, Artur F. Izmaylov, Julien Bloino, G. Zheng, J. L. Sonnenberg, M. Hada, M. Ehara, K. Toyota, R. Fukuda, J. Hasegawa, M. Ishida, T. Nakajima, Y. Honda, O. Kitao, H. Nakai, T. Vreven, J. A. Montgomery Jr., J. E. Peralta, François Ogliaro, Michael J. Bearpark, Jochen Heyd, E. N. Brothers, K. N. Kudin, V. N. Staroverov, Rika Kobayashi, J. Normand, Krishnan Raghavachari, Alistair P. Rendell, J. C. Burant, S. S. Iyengar, Jacopo Tomasi, M. Cossi, N. Rega, N. J. Millam, M. Klene, J. E. Knox, J. B. Cross, V. Bakken, C. Adamo, J. Jaramillo, R. Gomperts, R. E. Stratmann, O. Yazyev, A. J. Austin, R. Cammi, C. Pomelli, J. W. Ochterski, R. L. Martin, K. Morokuma, V. G. Zakrzewski, G. A. Voth, P. Salvador, J. J. Dannenberg, S. Dapprich, A. D. Daniels, Ö. Farkas, J. B. Foresman, J. V. Ortiz, J. Cioslowski, D. J. Fox, Gaussian 09, Revision E.01. Gaussian, Inc., 340 Quinnipiac St Bldg 40 Wallingford, CT 06492 USA, 2009.
[30] T. Yanai, D. P. Tew, N. C. Handy, *Chem. Phys. Lett.*, **2004**, DOI:10.1016/j.cplett.2004.06.011.
[31] P.-O. Widmark, P.-Å. Malmqvist, B. O. Roos, *Theor. Chim. Acta*, **1990**, DOI:10.1007/BF01120130.
[32] B. O. Roos, V. Veryazov, P.-O. Widmark, *Theor. Chem. Acc.*, **2004**, DOI:10.1007/s00214-003-0537-0.
[33] T. A. Keith, AIMAll (19.10.12), TK Gristmill Software, Overland Park KS, USA (http://aim.tkgristmill.com). TK Gristmill Software, Overland Park KS, USA, 2019.

[34] S. R. Kirk, S. Jenkins, QuantVec. BEACON Research Group, College of Chemistry and Chemical Engineering, Hunan Normal University, Changsha, Hunan, P.R. China, 2021.
[35] P. Ramachandran, G. Varoquaux, *Comput. Sci. Eng.*, **2011**, DOI:10.1109/MCSE.2011.35.